

Terahertz Communications Using Effective-Medium-Slot Waveguides

Nguyen H. Ngo,¹ Weijie Gao,¹ Guillaume Ducournau,² Hadjer Nihel Khelil,² Rita Younes,²

Pascal Sriftgiser,³ Hidemasa Yamane,⁴ Yoshiharu Yamada,⁴ Shuichi Murakami,⁴

Withawat Withayachumnankul,⁵ and Masayuki Fujita¹

¹⁾*Graduate School of Engineering Science, The University of Osaka, Toyonaka 560-8531, Japan*

²⁾*CNRS, UMR 8520 - IEMN, Institut d'Electronique de Microélectronique et de Nanotechnologie, Université de Lille, Lille 59000, France*

³⁾*Laboratoire de Physique des Lasers, Atomes et Molécules, UMR CNRS 8523 PhLAM, Université de Lille, Lille 59000, France*

⁴⁾*Osaka Research Institute of Industrial Science and Technology, Osaka 594-1157, Japan*

⁵⁾*Terahertz Engineering Laboratory, Adelaide University, Adelaide, SA 5005, Australia*

(*Electronic mail: ngo.h-nguyen.es@osaka-u.ac.jp)

(Dated: 13 January 2026)

All-dielectric effective-medium-clad waveguides have been widely exploited in terahertz communications owing to their extremely low loss, low dispersion, and broad bandwidth. In this work, we propose a substrateless effective-medium-slot waveguide. Additionally, we introduce a taper-free interface that allows terahertz waves to directly couple from a metallic hollow waveguide without requiring dielectric insertion. By engineering slot couplers with an effective-medium channel for impedance and modal matching, the waveguide achieves a fractional 3-dB bandwidth of 40% with a maximum coupling efficiency of 90% in the WR-2.2 band (330–500 GHz). By employing a broadband uni-traveling-carrier photodiode transmitter and sub-harmonic mixer receivers, we achieve an aggregated data rate of 0.8 Tbit/s with quadrature amplitude modulation schemes across 14 channels from 330–600 GHz. The effective-medium-slot waveguide platform yields robust broadband coupling with enhanced mechanical protection, offering reliable interconnects for ultra-high-speed terahertz integrated systems.

I. INTRODUCTION

In recent years, the rapid expansion in internet services has resulted in an exponential increase in data transfer volumes, with peak wireless data rates expected to exceed 100 Gbit/s in commercial systems by 2030.^{1–4} Based on Shannon's theory⁵, broader bandwidths can offer higher data capacity. Then, the growing demand for higher data rates is driving the adoption of terahertz frequencies in communications technologies (6G and beyond) owing to their broad spectra.^{6,7} With the availability of terahertz spectra around 300-GHz band,^{8,9} data rates exceeding 100 Gbit/s were achieved.^{10–12} More recently, an aggregated data rate over 1 Tbit/s was achieved in the 600-GHz band using a system of a photonic-based transmitter with an electronic receiver across 14 channels.¹³ However, this demonstration was limited to a back-to-back configuration, in which the transmitter and receiver were directly connected through a metallic hollow waveguide. The realization of higher data rates at frequencies above 300 GHz remains challenging due to the limited availability of high-performance terahertz sources, detectors, and low-loss, broadband interconnects.

Terahertz waves can be generated using several techniques, such as down-conversion of optical signals,¹⁴ frequency multiplication,^{15–17} and self-oscillation of semiconductor devices.^{18,19} For waveguiding purpose, the generated terahertz waves usually need to be coupled to various interconnects, such as metallic hollow waveguides, fibers, and dielectric-based waveguides, which can operate up to 1 THz or higher.²⁰ Notably, metallic hollow waveguides, in which most of the waves propagates in the air core, are widely used in commercial devices and lab demonstrations.²¹ With advanced micromachining processes, the size of waveguides

can be as small as 43 μm for operation frequencies up to 3 THz.^{22–24} However, the propagation loss in metallic waveguides, even with a gold-plating layer, becomes significant at such high frequencies due to dramatically reduced skin depths.²⁵ Although metallic waveguides are employed as a standard interconnect in terahertz electronics system, their flange design, which is usually fixed by standard rather than operation frequency. This makes them relatively bulky, occupying considerable space and limiting their applicability in large-scale integration.

As an alternative for on-chip integration, all-dielectric waveguides have proven effectiveness and scalability for terahertz applications. To eliminate substrate-induced dielectric loss and parasitic modes inherent to conventional platforms such as silicon-on-glass,²⁶ substrateless waveguide platforms were employed to enable intrinsically low-loss and well-confined terahertz waves.^{25,27–30} In particular, effective-medium-clad waveguides made of high-resistivity intrinsic silicon exhibited extremely high efficiency, low dispersion, and broad bandwidth.²⁸ They offer propagation losses as low as 0.05 dB/cm and a fractional bandwidth as large as 42.4%. Importantly, the effective-medium cladding formed by a periodic array of air holes can be modeled as a homogeneous material with tailororable permittivity tensor,^{28,31} resulting in the realization of various components for integrated terahertz devices,^{32–37} as illustrated in Fig. 1.

As an alternative to a solid silicon core, dielectric slot waveguides have attracted interest for their strong field confinement in a low-index region, low propagation loss, and simple fabrication.^{38–42} The fundamentals of dielectric slot waveguides were investigated in both optical^{38,43} and terahertz domains.⁴⁴ At high-index-contrast interfaces, continuity of the normal component of the electric displacement field enforces a strong electric-field (E -field) discontinuity, result-

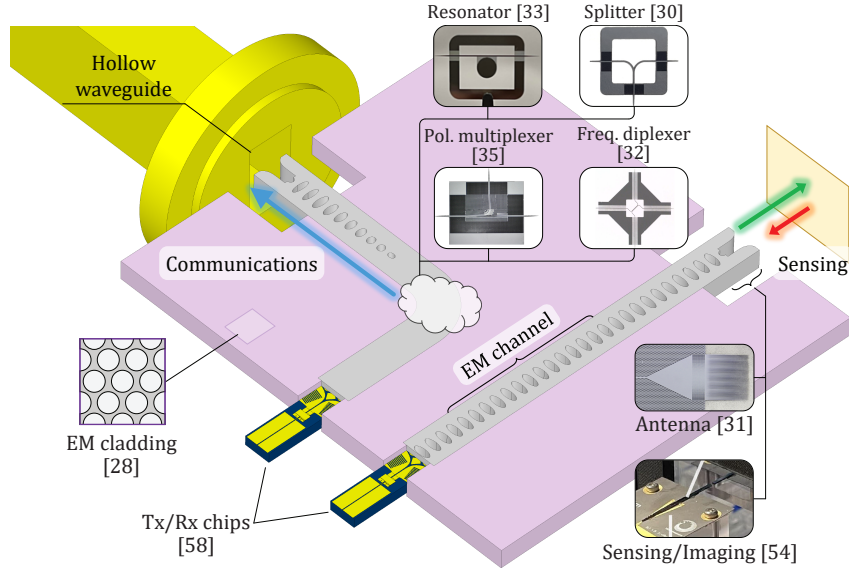


FIG. 1. Integrated all-silicon platform comprising effective-medium (EM)-slot waveguides. Active devices are coupled to the EM channel for sensing and communication applications. Ref. [54] is reproduced from Y. Kawamoto *et al.*, *IEEE Sens. J.* **25**, 20648–20657 (2025); licensed under a Creative Commons Attribution (CC BY) license.

ing in significant field enhancement and confinement of the guided mode within the low-index gap. The slot concept is applied in various passive components, such as antenna,^{44,45} coupler,^{46,47} and waveguides.^{36,48} Earlier, we demonstrated contact coupling by using a modified slot to minimize index mismatch at the interface with a metallic waveguide⁴⁹, achieving 32-Gbit/s error-free transmission by using on-off keying modulation. Nevertheless, an additional structure, i.e., photonic crystal slab, was required to enhance the coupling efficiency at low frequencies, which increased the design complexity.

In this work, we introduce a substrateless slot waveguide with an effective-medium structure, featuring robust coupling between silicon waveguide and hollow waveguide in the WR-2.2 band (330–500 GHz). The slot coupler is optimized to reduce the impedance and modal mismatch when connecting to the hollow waveguide, enhancing the coupling efficiency up to 90%. To realize the slot waveguide without a supporting substrate, the slot is substituted by an array of sub-wavelength elliptical air hole. This silicon-air structure forms an anisotropic low-index region, efficiently transferring the energy captured from the slot coupler. The developed substrateless slot waveguide is employed as a terahertz interconnect capable of operating beyond 500 GHz, and enabling a broad bandwidth for communications with aggregated data rates of up to 809 Gbit/s, thereby demonstrating its potential for ultra-high-speed data transmission. By incorporating compact terahertz transceivers,^{50,51} the waveguide architecture can be expected to support non-destructive sensing and imaging,^{52–54} facilitating integrated sensing and communication applications for 6G and beyond, as illustrated in Fig. 1.

Section II describes the design of the substrateless slot waveguide. Section III presents the validation of the fabricated samples and discusses the effective-medium-slot waveguide

with other existing waveguides in the terahertz range. Section IV demonstrates the broad bandwidth capability by supporting communications rates of 0.8 Tbit/s.

II. REVOLUTION OF THE WAVEGUIDE DESIGN

The proposed substrateless slot waveguide is conceptually divided into two functional sections: (i) an effective-medium channel that forms a low-index material of the slot and offers mechanical support for the dual silicon beams, and (ii) a slot coupler for taper-free coupling between the guiding channel and a metallic hollow waveguide. All structures are simulated using a full-wave simulator, CST Microwave Studio Suite. In each configuration, the dielectric waveguides are fed by metallic hollow waveguides via contact interfacing as a practical implementation. The operation frequency covers the WR-2.2 band. The design concepts are detailed as follows.

A. Effective-medium-slot waveguide

A bare slot waveguide is typically fabricated on a silicon-on-insulator platform. However, this configuration introduces additional absorption and radiation losses due to the wave leakage into the substrate. Moreover, the need for adhesive bonding⁴⁶ or heterogeneous material integration approach⁴² further increases fabrication complexity.

To this end, we propose a substrateless slot waveguide, as conceptualized in Fig. 2(a). A fundamental transverse-electric (TE) mode with in-plane polarization is excited, where the electric field E_x propagates along the z -direction. A central effective-medium channel acts as a low-index region to connect the two silicon beams, while additional effective-medium

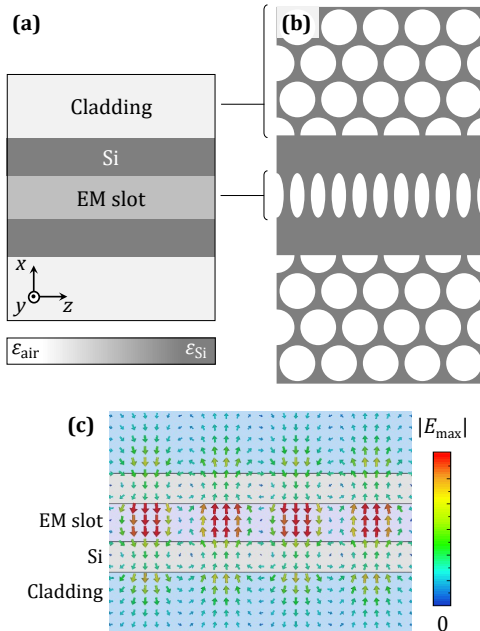


FIG. 2. Effective-medium (EM)-slot waveguide. (a) Representation of slot and cladding replaced by artificial anisotropic materials, (b) EM-slot waveguide based on air-silicon (Si) periodic structures. (c) Simulated instantaneous E -field vector distribution at 415 GHz.

claddings with refractive indices close to that of air are applied to the outer sides of the beams for wave confinement and handling purposes.²⁸

To realize an all-silicon substrateless structure, an effective medium in the form of elliptical air holes is introduced into the low-index region, as shown in Fig. 2(b). This air hole array also establishes a connection for the two silicon beams. Elliptical air holes are designed with a period d of 50 μm , which is approximately a quarter of the shortest wavelength in bulk silicon. The semi-minor axis r_{a1} and semi-major axis r_{b1} are 19.8 μm and 72 μm , respectively. This subwavelength-featured channel is therefore considered as an anisotropic material, where the relative permittivity tensor of the effective-medium slot $(\epsilon_x, \epsilon_y, \epsilon_z) = (3.65, 5.04, 3.65)$ is derived as follows^{28,36}:

$$\epsilon_x = \epsilon_z = \epsilon_{\text{Si}} \frac{(\epsilon_{\text{Si}} + \epsilon_0) + (\epsilon_0 - \epsilon_{\text{Si}})\zeta}{(\epsilon_{\text{Si}} + \epsilon_0) - (\epsilon_0 - \epsilon_{\text{Si}})\zeta}, \quad (1)$$

$$\epsilon_y = \epsilon_{\text{Si}} + (\epsilon_0 - \epsilon_{\text{Si}})\zeta, \quad (2)$$

$$\zeta = \frac{\pi r_{a1} r_{b1}}{2r_{b1}d}, \quad (3)$$

where $\epsilon_{\text{Si}} = 11.68$ and $\epsilon_0 = 1$ represent the relative permittivities of silicon and air, and ζ is the filling factor of air volume in silicon. Similarly, the relative permittivity tensor of the cladding, of which the period a_{clad} is 120 μm and radius r is 55 μm , is calculated as $(\epsilon_x, \epsilon_y, \epsilon_z) = (2.55, 3.54, 2.55)$. The relative permittivity tensors of the effective-medium slot and cladding are employed in the simulation model built from Fig. 2(a), showing that the guided mode is strongly confined within the effective-medium slot region, as illustrated

in Fig. 2(c). This approach effectively realizes a slot waveguide without relying on a conventional supporting substrate. By eliminating substrate-induced dielectric loss, the proposed structure enables high efficiencies for terahertz-wave propagation. Compared with conventional effective-medium-clad waveguides with solid cores, the proposed effective-medium-slot waveguide supports tighter modal confinement, offering the potential for increased circuit density.

B. Slot coupler

Metallic hollow waveguides are commonly used to excite terahertz dielectric waveguides. Figure 3(a) shows an in-plane cutaway view of the simple-slot waveguide coupling to hollow waveguides. The abrupt transition at the interface between the air at the hollow waveguide output and the silicon of the slot waveguide causes large modal and impedance mismatches, leading to significant fluctuations in transmission and reflection, as shown in Fig. 3(d). To facilitate an adiabatic modal transition, we introduce an apodized slot that incorporates an n^{th} -order polynomial taper with an offset of Δs and a total length l_{slot} , as shown in Fig. 3(b). This polynomial representation is advantageous because the curvature can be straightforwardly tuned by modifying the order n . Simultaneous optimization of the three parameters provides tight control over the slot curvature, thereby ensuring a smooth evolution of the modal index and the highest coupling efficiency. Moreover, the air gap g and beam width w are optimized so that the mode of the apodized slot is matched to that of the hollow waveguide at the silicon-air interface. This modification effectively confines the electric field within the slot region, thereby significantly reducing reflections and smoothing the coupling efficiency across the entire WR-2.2 band, as depicted in Fig. 3(e). The effective-medium structure, where dimensions of the air-hole array (E_1) is depicted in the previous subsection, is employed. To further improve modal and impedance matching between the effective-medium slot transition and the coupler, the first ellipse of the array (E_2) is adjusted with key parameters systematically optimized in Fig. 3(c). As a result, the transmission is enhanced with lower reflection, as depicted in Fig. 3(f).

The simulated E -field distributions in the substrateless slot waveguide at different frequencies are illustrated in Fig. 4(a). In the in-plane cross-section, the waves can efficiently couple into the slot and propagate along the elliptical air holes. As this effective-medium channel acts as a low-index region, the guided modes are tightly confined between the dual silicon beams with minimal leakage into the air cladding, as shown by the E -field intensity profile along the x -axis in Fig. 4(b). At high frequencies (e.g., 500 GHz), the guided mode exhibits stronger confinement in both in-plane and out-of-plane directions, resulting in high coupling efficiency of approximately -1 dB. In contrast, at the lower frequency bound, the weaker wave confinement in the out-of-plane direction arises from the longer wavelength, which prevents the slot from capturing the entire field energy. This effect, combined with the limited thickness of the 200- μm silicon wafer, leads to wave leakage

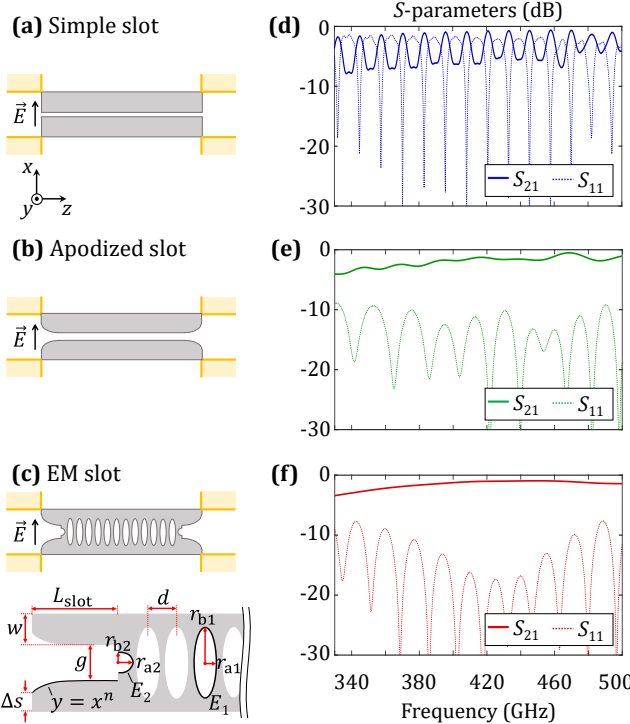


FIG. 3. In-plane cutaway views of slot-based silicon waveguides (gray) coupling to hollow rectangular waveguides (yellow): (a) Simple slot, (b) apodized slot, and (c) effective-medium (EM) slot waveguide with a magnified view. S -parameters of (d) simple-slot waveguide, (e) apodized-slot waveguide, and (f) EM-slot waveguide. Parameters of the magnified view of the EM-slot waveguide are given as: $w = 80 \mu\text{m}$, $g = 100 \mu\text{m}$, $l_{\text{slot}} = 150 \mu\text{m}$, $n = 6.6$, $\Delta s = 50 \mu\text{m}$; $d = 50 \mu\text{m}$, $r_{a1} = 19.8 \mu\text{m}$, $r_{b1} = 72 \mu\text{m}$, $r_{a2} = 24.5 \mu\text{m}$, $r_{b2} = 31.5 \mu\text{m}$.

and scattering into air, explaining the reduced coupling efficiency of -3.5 dB at 330 GHz , as shown in Fig. 3(f). Despite the slight degradation at lower frequencies, the simulated S -parameters suggest a wide 3-dB bandwidth of 170 GHz (41% fractional bandwidth) and an average coupling efficiency of -1.5 dB , which are sufficient for most terahertz applications such as high-speed communications. More importantly, the proposed design improves practical implementation by eliminating the fragile tapered spikes traditionally required for coupling with metallic hollow waveguides.

III. WAVEGUIDE CHARACTERIZATION

The waveguides with different lengths (1, 2, and 3 cm) are fabricated using the deep reactive ion etching (DRIE) process on a high-resistivity ($>10 \text{ k}\Omega\text{-cm}$) float-zone silicon wafer with a thickness of $200 \mu\text{m}$. In Figs. 5 (a-c), the fabrication quality is inspected using a microscope, revealing a tolerance of approximately 5%, confirming its high precision. To enable the proposed channel waveguide as an integrated platform for accommodating both passive and active components, we introduce effective-medium claddings surrounding the core, as shown in Fig. 5(d). Noticeably, the cladding is trimmed with

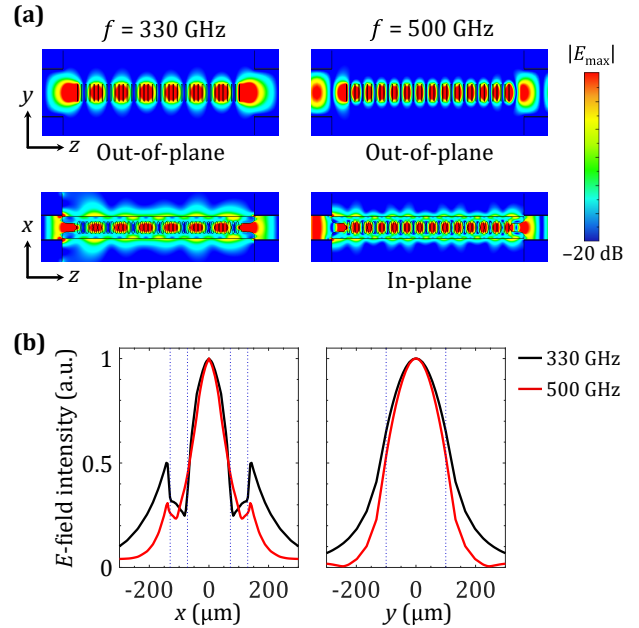


FIG. 4. Field plots for the proposed waveguide. (a) Out-of-plane and in-plane 2D E -field distributions of the substrateless slot waveguide at 330 GHz and 500 GHz . (b) Normalized E -field intensities along the x -axis and y -axis at 330 GHz and 500 GHz .

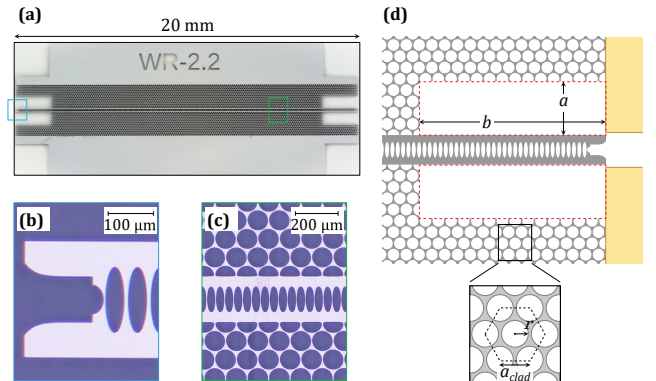


FIG. 5. Fabricated substrateless slot waveguide. (a) Fabricated sample with length of 20 mm . Magnified views of (b) slot coupler and (c) effective-medium slot, consisting of elliptical air holes. (d) Dimensions of the effective-medium claddings, where $a_{\text{clad}} = 120 \mu\text{m}$ and $r = 55 \mu\text{m}$. The red-dashed rectangles are trimmed from claddings to reduce the interference as waves couple from the hollow waveguide (yellow) to the slot. The dimensions are $a = 500 \mu\text{m}$ and $b = 2650 \mu\text{m}$.

a rectangular area so that the interference of the evanescent fields at the slot couplers is minimized. The vertical distance a between the slot and the cladding is $500 \mu\text{m}$, where the E -field intensity is negligible.

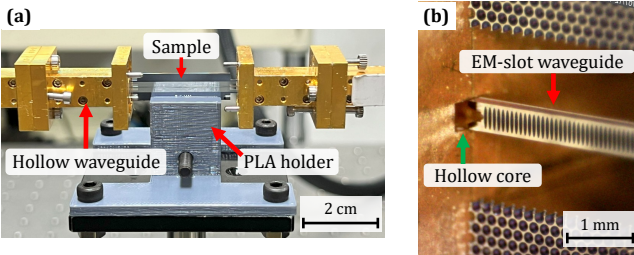


FIG. 6. Experimental setup for characterization. (a) Setup for the S-parameters measurement. (b) Magnified view at the interface between the slot coupler and the metallic hollow waveguide.

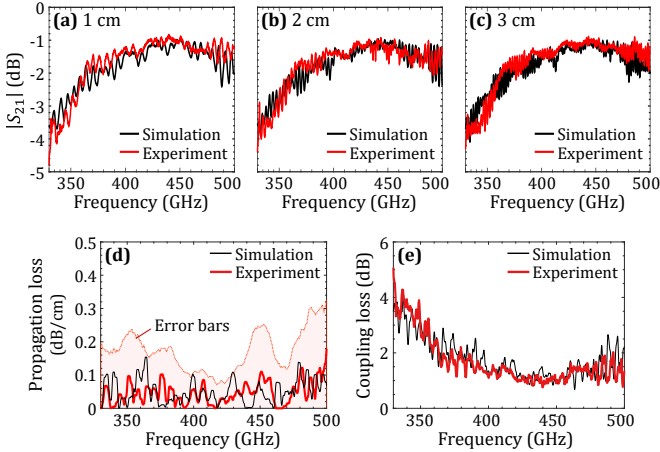


FIG. 7. Characteristics of the channel waveguide. Simulated and measured transmission coefficients at lengths of (a) 1 cm, (b) 2 cm, and (c) 3 cm. (d) Propagation loss with error bars. (e) Coupling loss.

A. Measurements and Results

The S-parameters are measured using a Keysight vector network analyzer (VNA) with VDI extenders operating at the WR-2.2 band. As shown in Fig. 6(a), the waveguide sample is secured using a 3D-printed holder and is directly in contact with the opening of the feeding hollow waveguides, as illustrated in Fig. 6(b). The alignment between the feed and the sample is finely adjusted using micropositioning stages. Figure 7(a-c) shows the coupling efficiencies of the channel waveguides for various lengths. Both the simulation and experimental results exhibit excellent agreements, validating the efficacy of the channel structure. The maximum and average coupling efficiencies of the 3-cm sample are -0.9 and -1.65 dB, respectively. The 3-dB bandwidth spans 165 GHz with a fractional bandwidth of 40%, ranging from 335 GHz to 500 GHz, covers almost the whole WR-2.2 band.

The propagation loss and coupling loss are extracted by comparing the transmission coefficients of the waveguides with various lengths. As shown in Fig. 7(d), the average and maximum propagation losses are 0.05 and 0.38 dB/cm, respectively, which are attributed to the low-loss characteristic of high-resistivity silicon. The presence of negative values in the propagation loss is primarily due to fluctuations in the

transmission coefficients caused by coupling between the dielectric and hollow waveguides. As shown in Fig. 7(e), the coupling loss ranges from 0.7 to 5 dB, with an average value of 1.7 dB across the WR-2.2 band. To reduce the coupling loss at a lower frequency range (<350 GHz), a larger aperture of the hollow waveguide, such as WR-2.8 ($711\text{ }\mu\text{m} \times 356\text{ }\mu\text{m}$), can be used to capture the field leakage, while the corresponding dielectric waveguide interface requires slight optimization to fit the larger aperture.

B. Discussions on slot-based waveguides

Table I compares performances of the proposed substrateless slot waveguide with previously reported terahertz dielectric waveguides coupled to metallic hollow waveguides. Waveguides with supporting substrates, typically based on silicon-on-insulator platforms, exhibit relatively high attenuation (>1.4 dB/cm), mainly due to substrate-induced absorption and radiation leakage.^{46,55} In contrast, substrateless waveguides fabricated from high-resistivity silicon demonstrate much lower propagation loss, with average values on the order of 0.1 dB/cm. Conventional dielectric waveguides require tapered transitions to achieve modal and impedance matching to metallic hollow waveguides.^{28,37,56} In the WR-3.4 band (220–330 GHz), the multimode interferometer waveguide reduces the insertion length from a conventional 3 mm to 0.26 mm by employing a trapezoidal slot coupler.⁴⁷ This coupler operates based on a quarter-wave matching principle, where reflections at the two slot interfaces destructively interfere. However, because the guided wavelengths at low frequencies exceed the interference range, the coupler must be inserted into the hollow core to suppress radiation leakage. To achieve an insertion-free coupling mechanism, we first designed taperless couplers using apodized-slot geometries to broaden the matching bandwidth to 36%.⁴⁹ Nevertheless, this structure still relies on subsequent tapered waveguides, leading to additional loss due to multiple mode-conversion stages. In contrast, the proposed slot waveguide employs an effective-medium channel for broadband modal matching, directly converting the mode from the slot coupler to the guiding channel without relying on auxiliary leakage-suppression structures, achieving a 40% fractional bandwidth.

It is worth noticed that conventional tapered-spike couplers demand alignment along all three Cartesian axes (x , y , and z). In contrast, our effective-slot waveguide geometry requires only x - y alignment, i.e., the alignment at the interface of the output of the hollow waveguide. Particularly, minor misalignment along the x -axis is no longer affected by silicon-metal interactions that would generate strong standing waves and dramatically degrade transmittance. The sensitivity to such misalignment is elaborated by simulations presented in *Supplement-S1*. Furthermore, the array of air holes can be transformed into a homogeneous silicon channel (no air holes) by gradually tapering the sizes of air holes (as described in *Supplement-S2*), making it compatible with silicon-integrated platforms^{33,35,36,57} and active devices,⁵⁸ while providing a robust interface with external hollow waveguide-based systems.

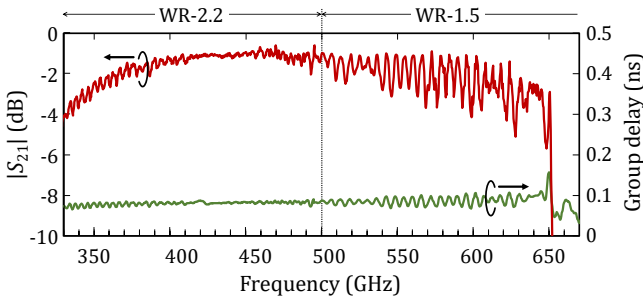


FIG. 8. Measured transmittance and group delay of the substrateless slot waveguide across the WR-2.2 (330–500 GHz) and WR-1.5 (500–750 GHz) bands.

Finally, packaging of this channel waveguide does not require metallic-hollow-waveguide interface,⁵⁹ enabling lower fabrication complexity and better scalability with 3D-printing technologies.⁶⁰

IV. BROADBAND WAVEGUIDE FOR HIGH-SPEED COMMUNICATIONS

In the previous section, the measured transmission coefficient showed that the operational bandwidth of the waveguide could extend toward higher frequencies. In order to fully exploit the available broad spectrum for communications, the waveguide is further characterized in the WR-1.5 band (500–750 GHz). Figure 8 presents the transmission coefficients and group delay of the channel waveguide across both the WR-2.2 and WR-1.5 bands. Ripples observed in the transmittance at high frequencies arise from the excitation of higher-order modes and increased impedance mismatch at the waveguide transitions. As the guided wavelength decreases, the effective-medium channel is no longer in the sub-wavelength regime, leading to increased modal dispersion in the guiding structure. Consequently, the ripples becomes noticeable above 500 GHz with an increase of the group delay. However, the results in Fig. 8 indicate that the structure remains well matched up to 600 GHz, corresponding to a fractional 3-dB bandwidth of 57% (335–600 GHz). This broadened bandwidth permits the allocation of multiple distinct carrier channels for communications with high-order vector modulation schemes, which is described in detail in the following subsection.

A. Experimental setup

As shown in Fig. 9, the setup is based on the same concept as the previously reported test system.¹³ On the transmitter side, two free-running tunable lasers in the C-band (1530–1560 nm) are used to generate an optical beat signal with a frequency difference in the terahertz band. One of the laser sources is vector-modulated by a data signal generated from an arbitrary waveform generator (AWG) using an optical IQ modulator. The modulated laser output is then combined with the other laser via a fiber coupler and subsequently amplified

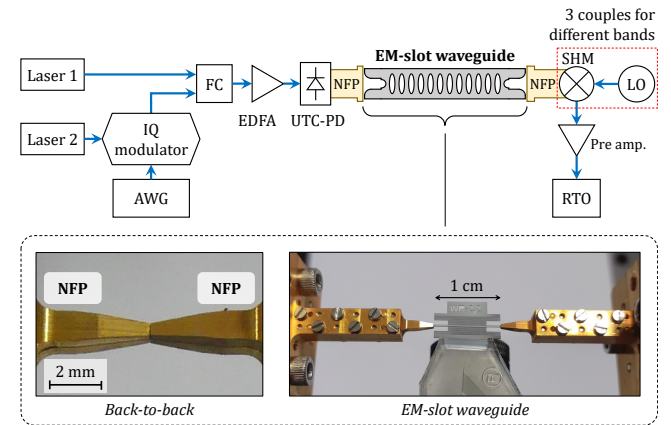


FIG. 9. Block diagram of communications with I/Q modulation. Near-field probes (NFP) for WR-2.2 band are fixed for all carrier frequencies. On the receiver side, three sets of sub-harmonic mixer/local oscillator (SHM/LO) couples are used to cover multiple channels. AWG: arbitrary waveform generator, FC: fiber coupler, EDFA: erbium-doped fiber amplifier, UTC-PD: uni-traveling carrier photodiode, RTO: real-time oscilloscope.

by an erbium-doped fiber amplifier (EDFA). Subsequently, the combined optical signal is photomixed by a uni-traveling carrier photodiode (UTC-PD)⁶¹ to generate a terahertz signal (330–600 GHz), which is then coupled to a WR-2.2 near-field probe (NFP). The NFP is used to feed the silicon waveguide and kept constant for all carrier frequencies.

On the receiver side, a subharmonic mixer (SHM) is used to demodulate the transmitted signal. The SHM is pumped with a local oscillator (LO) close to half of the carrier frequency. This LO signal is produced by a signal generator (SMA100B from Rohde & Schwarz) with a subsequent frequency multiplier. The resulting intermediate frequency (IF) singal, below 40 GHz, falls within the detection bandwidth of a 70-GHz real-time oscilloscope (UXR, Keysight). Signal demodulation is performed using Keysight's Vector Signal Analysis (VSA) software.⁶² Digital processing in the VSA includes equalization through digital filtering to compensate for the system's frequency-dependent response, particularly the roll-off effect of the SHM.

B. I/Q modulated communications with multiple channels

The frequency range is determined by the broadband response of the channel waveguide, spanning from 330 GHz carrier up to 600 GHz, as shown in the Fig. 10(a). In order to fully exploit this wide spectrum for communications, 14 channels are allocated at various carrier frequencies, as listed in Table II. While the lasers are tuned to change the carrier frequency emitted by the photonic-based transmitter, a set of three receivers is used to cover the broad terahertz bandwidth. The first receiver is a WR-2.2 subharmonic mixer (SHM), enabling the detection of channels 1~8 (330 to 470 GHz). The second receiver, used for channels 9~11, covers 480 to 550 GHz (carriers 490/515/540 GHz) is composed of SHM in-

TABLE I. Comparison of terahertz silicon waveguides coupled to metallic hollow waveguides, sorted by insertion length.

Waveguide type	Frequency (GHz)	3-dB bandwidth (%)	Propagation loss (Average/Max) (dB/cm)	$ S_{21} _{\max}$ (dB)	Insertion length (mm)
With supporting substrate					
SIIG WG ⁵⁵	215–335	44	1.43 / -	-2	2.72
Slot WG on a SBQ platform ⁴⁶	500–570	13	1.68 / 4	-2.9	0.75
MEMS slot WG ⁴⁴	224–326	37	1.5 / -	-11	0
Substrateless					
Photonic crystal WG ⁵⁶	322–350	8	<0.05 / 0.1	~0	6
Effective-medium-cladded WG ²⁸	260–390	42	0.05 / 0.09	-0.1	3
Extreme skin-depth WG ³⁷	220–330	40	0.1 / 0.37	-0.05	2.7
MMI WG ⁴⁷	237–325	31.3	-	-0.3	0.26
Taperless-interfaced WG ⁴⁹	349–500	36	-	-1.0	0
This work	335–500	40	0.05 / 0.38	-0.9	0

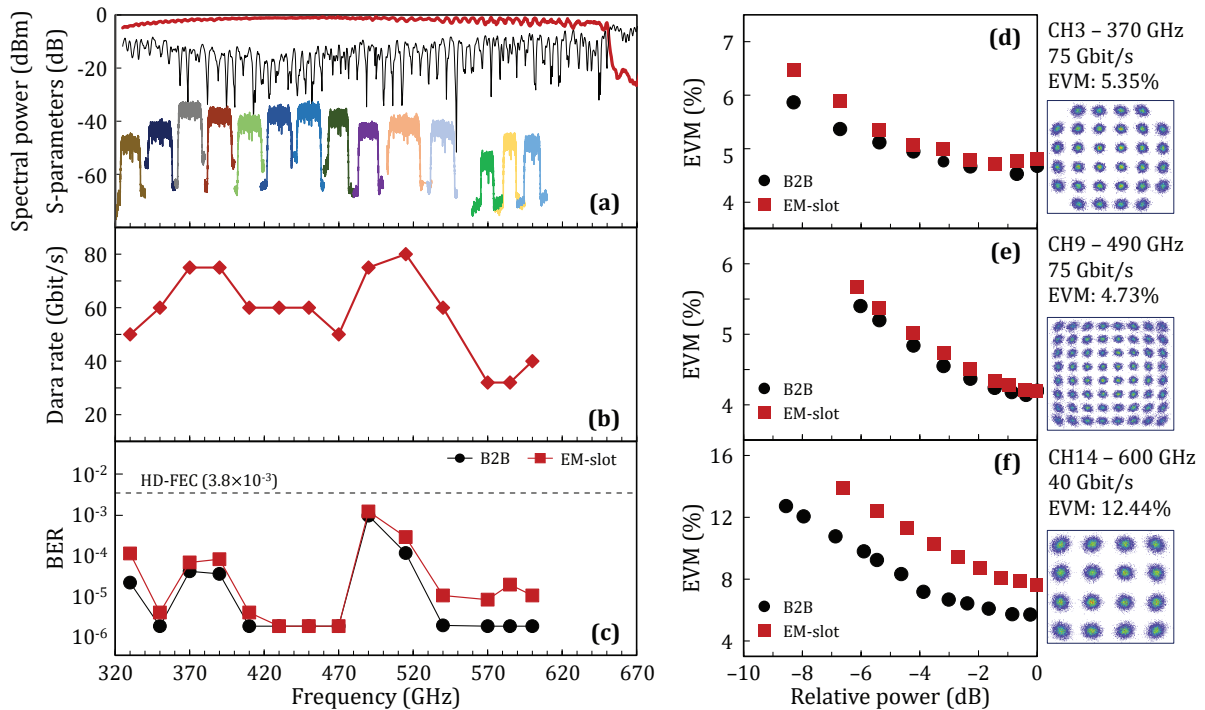


FIG. 10. Communications performance. (a) Measured absolute received power spectra at 14 allocated frequencies. S-parameters are also embedded. (b) Data rate of 14 channels, with aggregated data rate of 809 Gbit/s. Maximum/minimum: 80/32 Gbit/s. (c) BER at each carrier frequency for back-to-back and with effective-medium (EM)-slot waveguide. EVM versus relative transmitted power of back-to-back (black circles) and with EM-slot waveguide (red squares) at (d) 370 GHz (channel 3, 32-QAM), (e) 490 GHz (channel 9, 64-QAM), and (f) 600 GHz (channel 14, 16-QAM). Constellation diagram at corresponding EVM are also included. Relative power: power variation with respect to the maximum power used for each carrier.

tegrated in a WR-1.9 (400–600 GHz) waveguide. The last receiver is a WR-1.5 SHM, to cover the last 3 channels (12~14) corresponding to the 570/585/600 GHz carriers.

Each carrier frequency is tested in two configurations. First, the “back-to-back” case, where the near-field probes of the

transmitter and receiver are in direct contact, sets the reference performance in terms of the error-vector magnitude (EVM) metric.⁶³ Second, the effective-medium slot waveguide is employed in the system and the EVM performance is measured again. Several quadrature amplitude modulation (QAM) for

TABLE II. Frequency allocation, modulation types, and data rates of 14 channels. Aggregated data rate: 809 Gbit/s.

SHM's band		WR-2.2								WR-1.9			WR-1.5		
Channel		1	2	3	4	5	6	7	8	9	10	11	12	13	14
f_c (GHz)		330	350	370	390	410	430	450	470	490	515	540	570	585	600
Mod. type (-QAM)		16	16	32	32	16	16	16	16	64	16	16	16	16	16
Power penalty (dB)		3.5	3.1	1.3	2.2	1.9	1.6	1.0	1.9	1.0	1.4	2.2	4.1	3.9	3.1
Data rate (Gbit/s)		50	60	75	75	60	60	60	50	75	80	60	32	32	40
EVM (%)		8.5	7.5	5.1	5.0	7.3	6.8	6.2	7.0	4.2	9.3	7.4	7.4	8.0	7.6

mats are used to assess the performance of the channel waveguide, consisting of 16-QAM, 32-QAM, and 64-QAM. Figure 10(b) shows the maximum data rate that the channel waveguide can support at each carrier frequency. The achievable data rate ranges from 32 to 80 Gbit/s, resulting in the aggregated throughput of 809 Gbit/s, enabling the potential of the waveguide for ultra-high-speed terahertz interconnects. Noticeably, the data rates measured with the WR-1.5 SHM are the lowest, likely due to the ripples observed in the transmittance and group delay around 600 GHz, as shown in Fig. 8. Despite the degradation, optimum bit-error rates (BER) remain below the hard-decision forward-error-correction (HD-FEC) limit ($BER < 3.8 \times 10^{-3}$), as shown in Fig. 10(c). For 16-QAM modulation, both configurations achieve BER values well below the HD-FEC threshold. For higher-order modulations (32-QAM and 64-QAM), a slight degradation is observed even in the reference measurement, primarily attributed to the limitations of the experimental testbed rather than the intrinsic response of the channel waveguide. Figures 10(d-f) show the EVM performance versus relative power at the transmitter of the channel waveguide and the back-to-back at three carrier frequencies (370/490/600 GHz). The relative power is defined as the power variation with respect to the maximum power used for each carrier, and the power penalty is extracted as the relative power variation required to achieve the same EVM as the back-to-back case. The measured power penalty ranges from 1 to 4 dB, which is consistent with the transmittance characteristics of the waveguide. In all cases, the channel waveguide exhibits good performance with a limited EVM degradation, as shown in Table II.

Table III compares the high-speed communication performance of state-of-the-art all-dielectric terahertz interconnects from 0.1 to 1 THz. A valley photonic-crystal waveguide demonstrates a data rate of 108 Gbit/s, yet their bandwidth is only about 30 GHz (~10% fractional bandwidth) owing to intrinsic photonic-bandgap dispersion.⁶⁶ In contrast, effective-medium-based waveguides support much broader bandwidths (approximately 40%), and deliver single-link data rates up to 100 Gbit/s. Most demonstrations, however, remain below 350 GHz, limited by the availability of efficient transmitters at higher frequencies. With the advent of the 600-GHz UTC-PD source, back-to-back transmission through WR-1.5 hollow waveguides has surpassed 1 Tbit/s.¹³ Building on these advances, our channel waveguide fully exploits its ultra-broadband characteristics to accommodate 14 channels with

BER below the HD-FEC threshold, enabling aggregate data rates of 809 Gbit/s from 330 GHz to 600 GHz, paving the way for 6G and beyond applications. Further optimization of the waveguide geometry in the extended frequency band is expected to reduce waveguide dispersion and reflection losses, targeting terabit-per-second terahertz communication.

V. CONCLUSION

We have proposed a substrateless slot waveguide along with an effective coupler to interface with rectangular waveguides. A transition of a slot coupler is modified for modal and impedance matching, resulting in strong *E*-field confinement within the air gap. An effective-medium slot formed by an elliptical air-hole array is introduced for connecting two beams of the slot coupler and emulating an air-like refractive index. This platform offers broadband and low-loss characteristics, enabling high-capacity terahertz communications. The waveguide is experimentally validated in the WR-2.2 band, exhibiting an average propagation loss of 0.05 dB/cm and a maximum coupling efficiency of 90%, and maintains good matching up to 600 GHz. Leveraging this wide operational bandwidth, data transmission through multiple channels, spanning 330–600 GHz, is demonstrated using a broadband UTC-PD as a transmitter with three SHM receivers for different frequency bands. By using QAM, the channel waveguide exhibits high data rate with limited EVM degradation, achieving an aggregate data rate of 0.8 Tbit/s with the BER below the HD-FEC limit for all channels. The interface is also robust to misalignment compared with a conventional tapered spike, yielding an efficient approach for packaging dielectric waveguide. Furthermore, the elliptical air holes can be progressively tapered,⁴⁸ transforming the effective-medium channel into various passive components. This versatility enables efficient interconnection for ultra-high-speed communications and integrated sensing, as conceptualized in Fig. 1, paving the way for applications toward 6G and beyond.

ACKNOWLEDGMENTS

This work was supported in part by the JST Core Research for Evolutional Science and Technology (JPMJCR21C4), the Grants-in-Aid for Scientific Research (24H00031), and

TABLE III. State-of-the-art all-dielectric devices for terahertz communications, sorted by data rates.

Interconnect	Frequency (GHz)	Tx	Rx	Distance (mm)	Modulation	No. of channels	Data rate (Gbit/s)		BER
							Max*	Total	
Single channel									
EM WG ²⁸	335	UTC-PD	SBD	30	OOK	1	28	28	9×10^{-12}
PC WG ⁶⁴	350	UTC-PD	RTD	6	OOK	1	32	32	2×10^{-12}
Paperless WG ⁴⁹	350	UTC-PD	RTD	20	OOK	1	32	32	9×10^{-12}
EM WG (on-chip) ⁶⁵	315	UTC-PD	RTD	50	32-QAM	1	100	100	3.6×10^{-3}
VPC WG ⁶⁶	317	UTC-PD	SHM	10	16-QAM	1	108	108	7.4×10^{-4}
Multiple channels									
Multi-mode WG ⁶⁷	165	CMOS	CMOS	52	OOK	3	24	65	10^{-12}
Diplexer VPC WG ⁶⁸	305 321.6	UTC-PD	SHM	38	32-QAM	2	75	150	5×10^{-3}
Polarization multiplexer ³⁵	310	UTC-PD	FMBD	20	16-QAM	2	80 100	155 190	$< 3.6 \times 10^{-3}$ $< 2.0 \times 10^{-2}$
Hollow WG ¹³	500–724	UTC-PD	SHM	B2B	16,32,64-QAM	12 14	100 120	887 1,041	$< 8.0 \times 10^{-4}$ $< 8.3 \times 10^{-3}$
This work	330–600	UTC-PD	SHM	10	16,32,64-QAM	14	80	809	$< 1.2 \times 10^{-3}$

*Maximum data rate of a single channel.

WG: waveguide; EM: effective-medium clad; PC: photonic crystal; VPC: valley photonic crystal;

SBD: Schottky barrier diode; RTD: resonant tunneling diode; FMBD: Fermi-level managed barrier diode; SHM: sub-harmonic mixer. B2B: Back-to-back.

the Australia-Japan Foundation, Australia (AJF2021044). G.D. and P.S. state that the characterization testbeds are supported by France 2030 programs, PEPR (Programmes et Equipements Prioritaires pour la Recherche) and CPER Wavetech. The PEPR is operated by the Agence Nationale de la Recherche (ANR), under the grants ANR-22-PEEL-0006 (FUNTERA, PEPR ‘Electronics’) and ANR-22-PEFT-0006 (NF-SYSTERA, PEPR 5G and beyond - Future Networks). The ANR project PICOTE (ANR-23-CE24-0023) also supported the development of the 600 GHz testbed. The Contrat de Plan Etat-Region (CPER) WaveTech is supported by the Ministry of Higher Education and Research, the Hauts-de-France Regional council, the Lille European Metropolis (MEL), the Institute of Physics of the French National Centre for Scientific Research (CNRS) and the European Regional Development Fund (ERDF). The authors acknowledge support from CDP C2EMPI, the French State under the France-2030 program, the University of Lille, the Initiative of Excellence of the University of Lille, the European Metropolis of Lille for their funding and support of the R-CDP-24-004-C2EMPI project.

REFERENCES

¹Cisco, *Cisco Annual Internet Report (2018–2023)*, available at <https://www.cisco.com/c/en/us/solutions/collateral/executive-perspectives/annual-internet-report/white-paper-c11-741490.html> (accessed: 11 January 2026).

²Ericsson, *Mobile Data Traffic Outlook*, available at <https://www.ericsson.com/en/reports-and-papers/mobility-report/dataforecasts/mobile-traffic-forecast> (accessed: 11 January 2026).

³NTT DOCOMO, Inc., *White Paper: 5G Evolution and 6G (ver. 5.0)*, (January 2023), available at https://www.nttdocomo.ne.jp/english/corporate/technology/whitepaper_6g (accessed: 11 January 2026).

⁴Samsung Research, *6G: The Next Hyper-Connected Experience*, (July 2020), available at https://cdn.codeground.org/nsr/downloads/researchareas/20201201_6G_Vision_web.pdf (accessed: 11 January 2026).

⁵C. Shannon, “Communication in the presence of noise,” *Proceedings of the IRE* **37**, 10–21 (1949).

⁶M. Fujita, “Advanced terahertz devices and systems toward 6G and beyond,” in *2021 8th NAFOSTED Conference on Information and Computer Science (NICS)* (2021) pp. 348–351.

⁷T. Kurner, D. M. Mittleman, and T. Nagatsuma, eds., *THz Communications: Paving the Way Towards Wireless Tbps* (Springer, 2021).

⁸V. Petrov, T. Kurner, and I. Hosako, “IEEE 802.15.3d: First standardization efforts for sub-terahertz band communications toward 6G,” *IEEE Commun. Mag.* **58**, 28–33 (2020).

⁹International Telecommunication Union (ITU), *Technology Trends of Active Services in the Frequency Range 275–3000 GHz*, Report ITU-R SM.2352-1 (2022).

¹⁰K. Maekawa, T. Yoshioka, T. Nakashita, T. Ohara, and T. Nagatsuma, “Single-carrier 220-Gbit/s sub-THz wireless transmission over 214 m using a photonics-based system,” *Opt. Lett.* **49**, 4666–4668 (2024).

¹¹S. Jia, M.-C. Lo, L. Zhang, O. Ozolins, A. Udalcovs, D. Kong, X. Pang, R. Guzman, X. Yu, S. Xiao, S. Popov, J. Chen, G. Carpintero, T. Morioka, H. Hu, and L. K. Oxenløwe, “Integrated dual-laser photonic chip for high-purity carrier generation enabling ultrafast terahertz wireless communications,” *Nat. Commun.* **13**, 1388 (2022).

¹²A. Kumar, M. Gupta, P. Pitchappa, N. Wang, P. Sriftgiser, G. Ducournau, and R. Singh, “Phototunable chip-scale topological photonics: 160 Gbps waveguide and demultiplexer for THz 6G communication,” *Nat. Commun.* **13**, 5404 (2022).

¹³G. Ducournau, P. Sriftgiser, Y. Kawamoto, W. Gao, A. S. Mohammed, M. Zegaoui, M. Zaknoune, and T. Nagatsuma, "Photonics-enabled 1.04-Tbit/s aggregated data-rate in the 600-GHz-band," in *2023 Asia-Pacific Microwave Conference (APMC)* (2023) pp. 327–329.

¹⁴T. Ishibashi and H. Ito, "Uni-traveling-carrier photodiodes," *J. Appl. Phys.* **127**, 31101 (2020).

¹⁵H. Liu, Z. Liang, J. Meng, Y. Liu, H. Wang, C. Yan, Z. Wu, Y. Liu, D. Zhang, X. Wang, and B. Zhang, "120 GHz frequency-doubler module based on GaN Schottky barrier diode," *Micromachines* **13** (2022).

¹⁶Y. Zhang, C. Wu, X. Liu, L. Wang, C. Dai, J. Cui, Y. Li, and N. Kinar, "The development of frequency multipliers for terahertz remote sensing system," *Remote Sens.* **14** (2022).

¹⁷J. V. Siles, K. B. Cooper, C. Lee, R. H. Lin, G. Chattopadhyay, and I. Mehdi, "A new generation of room-temperature frequency-multiplied sources with up to 10x higher output power in the 160-GHz–1.6-THz range," *IEEE Trans. Terahertz Sci. Technol.* **8**, 596–604 (2018).

¹⁸Y. Nishida, N. Nishigami, S. Diebold, J. Kim, M. Fujita, and T. Nagatsuma, "Terahertz coherent receiver using a single resonant tunnelling diode," *Sci. Rep.* **9**, 18125 (2019).

¹⁹D. Cimbra, J. Wang, A. Al-Khalidi, and E. Wasige, "Resonant tunneling diodes high-speed terahertz wireless communications - A review," *IEEE Trans. Terahertz Sci. Technol.* **12**, 226–244 (2022).

²⁰R. A. S. D. Koala, M. Fujita, and T. Nagatsuma, "Nanophotonics-inspired all-silicon waveguide platforms for terahertz integrated systems," *Nanophotonics* **11**, 1741–1759 (2022).

²¹H. Ito, N. Shibata, T. Nagatsuma, and T. Ishibashi, "Terahertz-wave detector on silicon carbide platform," *Appl. Phys. Express* **15**, 26501 (2022).

²²Virginia Diodes, Inc., *Passive Components*, available at <https://vadiodes.com/passive-components/> (accessed: 11 January 2026).

²³B. Bulcha, J. Hesler, V. Drakinskiy, J. Stake, and N. Barker, "1.9–3.2 THz Schottky based harmonic mixer design and characterization," in *2015 European Microwave Conference (EuMC)* (2015) pp. 837–840.

²⁴B. T. Bulcha, J. L. Hesler, V. Drakinskiy, J. Stake, A. Valavanis, P. Dean, L. H. Li, and N. S. Barker, "Design and characterization of 1.8–3.2 THz Schottky-based harmonic mixers," *IEEE Trans. Terahertz Sci. Technol.* **6**, 737–746 (2016).

²⁵D. Headland, M. Fujita, G. Carpentero, T. Nagatsuma, and W. Withayachumankul, "Terahertz integration platforms using substrateless all-silicon microstructures," *APL Photon.* **8**, 91101 (2023).

²⁶N. Ranjesh, M. Basha, A. Taeb, and S. Safavi-Naeini, "Silicon-on-glass dielectric waveguide–Part II: For THz applications," *IEEE Trans. Terahertz Sci. Technol.* **5**, 280–287 (2015).

²⁷K. Tsuruda, M. Fujita, and T. Nagatsuma, "Extremely low-loss terahertz waveguide based on silicon photonic-crystal slab," *Opt. Express* **23**, 31977–31990 (2015).

²⁸W. Gao, X. Yu, M. Fujita, T. Nagatsuma, C. Fumeaux, and W. Withayachumankul, "Effective-medium-cladded dielectric waveguides for terahertz waves," *Opt. Express* **27**, 38721–38734 (2019).

²⁹Y. Yang, Y. Yamagami, X. Yu, P. Pitchappa, J. Webber, B. Zhang, M. Fujita, T. Nagatsuma, and R. Singh, "Terahertz topological photonics for on-chip communication," *Nat. Photon.* **14**, 446–451 (2020).

³⁰D. Headland, W. Withayachumankul, X. Yu, M. Fujita, and T. Nagatsuma, "Unclad microphotonics for terahertz waveguides and systems," *J. Lightwave Technol.* **38**, 6853–6862 (2020).

³¹W. Withayachumankul, R. Yamada, M. Fujita, and T. Nagatsuma, "All-dielectric rod antenna array for terahertz communications," *APL Photon.* **3**, 051707 (2018).

³²Y. Kawamoto, T. Yoshioka, N. Shibata, D. Headland, M. Fujita, R. Koma, R. Igarashi, K. Hara, J. ichi Kani, and T. Nagatsuma, "300-GHz-band diplexer for frequency-division multiplexed wireless communication," *IEICE Trans. Electron.* **E106.C**, 722–726 (2023).

³³P. Dechwechprasit, R. T. Ako, S. Sriram, C. Fumeaux, and W. Withayachumankul, "Terahertz disk resonator on a substrateless dielectric waveguide platform," *Opt. Lett.* **48**, 4685–4688 (2023).

³⁴W. Wang, Y. J. Tan, T. C. Tan, A. Kumar, P. Pitchappa, P. Sriftgiser, G. Ducournau, and R. Singh, "On-chip topological beamformer for multi-link terahertz 6G to XG wireless," *Nature* **632**, 522–527 (2024).

³⁵W. Gao, M. Fujita, S. Murakami, T. Nagatsuma, C. Fumeaux, and W. Withayachumankul, "Ultra-wideband terahertz integrated polarization multiplexer," *Laser Photonics Rev.* **19**, 2400270 (2025).

³⁶L. Chen, W. Gao, C. Fumeaux, and W. Withayachumankul, "Terahertz integrated polarization filter based on slotted bragg grating," *IEEE Trans. Terahertz Sci. Technol.* , 1–8 (2024).

³⁷H. Lees, D. Headland, and W. Withayachumankul, "Terahertz extreme skin-depth waveguides," *IEEE Trans. Terahertz Sci. Technol.* **14**, 758–767 (2024).

³⁸V. R. Almeida, Q. Xu, C. A. Barrios, and M. Lipson, "Guiding and confining light in void nanostructure," *Opt. Lett.* **29**, 1209–1211 (2004).

³⁹M. Nagel, A. Marchewka, and H. Kurz, "Low-index discontinuity terahertz waveguides," *Opt. Express* **14**, 9944–9954 (2006).

⁴⁰S. Atakaramians, S. A. V., T. M. Monroe, and D. Abbott, "Terahertz dielectric waveguides," *Adv. Opt. Photonics* **5**, 169–215 (2013).

⁴¹H.-T. Zhu, Q. Xue, J.-N. Hui, and S. W. Pang, "Design, fabrication, and measurement of the low-loss SOI-based dielectric microstrip line and its components," *IEEE Trans. Terahertz Sci. Technol.* **6**, 696–705 (2016).

⁴²J. R. Rodrigues, U. D. Dave, A. Mohanty, X. Ji, I. Datta, S. Chaitanya, E. Shim, R. Gutierrez-Jauregui, V. R. Almeida, A. Asenjo-Garcia, and M. Lipson, "All-dielectric scale invariant waveguide," *Nat. Commun.* **14**, 6675 (2023).

⁴³P. Steglich, "Silicon-on-Insulator slot waveguides: Theory and applications in electro-optics and optical sensing," in *Emerging Waveguide Technology*, edited by K. Y. You (IntechOpen, London, 2018) Chap. 10.

⁴⁴J. Barowski, L. Schmitt, K. Dausien, and M. Hoffmann, "Design, simulation, and characterization of mems-based slot waveguides," *IEEE Trans. Microw. Theory Techn.* **71**, 3819–3828 (2023).

⁴⁵D. Headland, A. Kumar, H. Lees, W. Withayachumankul, and G. Carpentero, "Matched dielectric slot waveguide as an all-dielectric terahertz magnetic dipole," *Opt. Lett.* **49**, 1361–1364 (2024).

⁴⁶H. Amarloo and S. Safavi-Naeini, "Terahertz slot dielectric waveguide implemented on the Silicon-BCB-Quartz platform," *IEEE Trans. Terahertz Sci. Technol.* **11**, 310–317 (2021).

⁴⁷D. Headland and G. Carpentero, "Robust unclad terahertz waveguides and integrated components enabled by multi-mode effects and matched slot couplers," *IEEE Trans. Terahertz Sci. Technol.* **15**, 885–893 (2025).

⁴⁸D. Headland, A. K. Klein, M. Fujita, and T. Nagatsuma, "Dielectric slot-coupled half-Maxwell fisheye lens as octave-bandwidth beam expander for terahertz-range applications," *APL Photon.* **6**, 096104 (2021).

⁴⁹N. H. Ngo, W. Gao, M. Li, W. Withayachumankul, and M. Fujita, "Terahertz slot waveguide for taperless interfacing," in *2024 49th International Conference on Infrared, Millimeter, and Terahertz Waves (IRMMW-THz)* (2024) pp. 1–2.

⁵⁰H. Hamada, T. Fujimura, I. Abdo, K. Okada, H.-J. Song, H. Sugiyama, H. Matsuzaki, and H. Nosaka, "300-GHz, 100-Gb/s InP-HEMT wireless transceiver using a 300-GHz fundamental mixer," in *2018 IEEE/MTT-S International Microwave Symposium - IMS* (2018) pp. 1480–1483.

⁵¹S. Suzuki and M. Asada, "Fundamentals and recent advances of terahertz resonant tunneling diodes," *Appl. Phys. Express* **17**, 070101 (2024).

⁵²L. Yi, Y. Li, and T. Nagatsuma, "Photonic radar for 3D imaging: From millimeter to terahertz waves," *IEEE J. Sel. Top. Quantum Electron.* **29**, 1–14 (2023).

⁵³H. Lees, D. Headland, S. Murakami, M. Fujita, and W. Withayachumankul, "Terahertz radar with all-dielectric leaky-wave antenna," *APL Photon.* **9**, 036107 (2024).

⁵⁴Y. Kawamoto, D. C. Gallego, A. Rivera-Lavado, T. Nagatsuma, M. Nagel, D. Headland, and G. Carpentero, "Near-field semiconductor imaging and classification enabled by signal cancellation using truncated mm-Wave silicon waveguide," *IEEE Sens. J.* **25**, 20648–20657 (2025).

⁵⁵M. Moradi, M. S. Sharawi, and K. Wu, "Exploring low-loss wideband substrate-integrated image guides (SIIG) for terahertz applications," *IEEE Trans. Terahertz Sci. Technol.* **14**, 1–12 (2024).

⁵⁶X. Yu, M. Sugeta, Y. Yamagami, M. Fujita, and T. Nagatsuma, "Simultaneous low-loss and low-dispersion in a photonic-crystal waveguide for terahertz communications," *Appl. Phys. Express* **12**, 12005 (2019).

⁵⁷W. Gao, W. Withayachumankul, M. Fujita, and T. Nagatsuma, "Terahertz integrated polarization rotator based on effective-medium-clad waveguide," in *2023 48th International Conference on Infrared, Millimeter, and Terahertz Waves (IRMMW-THz)* (2023) pp. 1–2.

⁵⁸N. H. Ngo, Y. Inose, Y. Nishida, R. Koala, Y. Matsuura, S. Murakami, Y. Yamada, H. Yamane, T. Nagatsuma, and M. Fujita, "Fusion of resonant tunneling diodes and terahertz silicon photonics for interconnects," in *2024*

IEEE Photonics Conference (IPC) (2024) pp. 1–2.

⁵⁹N. H. Ngo, W. Gao, M. Li, D. Ichikawa, W. Withayachumnankul, and M. Fujita, “Non-metallic 3D-printed packages based on dielectric slot waveguides,” in *2024 IEEE Conference on Antenna Measurements and Applications (CAMA)* (2024) pp. 1–2.

⁶⁰W. Gao, W. Withayachumnankul, M. Fujita, and T. Nagatsuma, “3D printed terahertz lens antenna fed by effective-medium-clad dielectric waveguide,” in *2023 XXXVth General Assembly and Scientific Symposium of the International Union of Radio Science (URSI GASS)* (2023) pp. 1–4.

⁶¹T. Nagatsuma, T. Kurokawa, M. Sonoda, T. Ishibashi, M. Shimizu, and K. Kato, “600-ghz-band waveguide-output uni-traveling-carrier photodiodes and their applications to wireless communication,” in *2018 IEEE/MTT-S International Microwave Symposium - IMS* (2018) pp. 1180–1183.

⁶²Keysight, *Vector Signal Analysis (89600 VSA Software)*, available at <https://www.keysight.com/us/en/products/software/pathwave-test-software/89600-vsa-software.html> (accessed: 11 January 2026).

⁶³Keysight, *EVM (Digital Demod)*, available at https://helpfiles.keysight.com/csg/89600B/Webhelp/Subsystems/digdemod/content/digdemod_symtblerrdata_evm.htm (accessed: 11 January 2026).

⁶⁴X. Yu, J.-Y. Kim, M. Fujita, and T. Nagatsuma, “Efficient mode converter to deep-subwavelength region with photonic-crystal waveguide platform for terahertz applications,” *Opt. Express* **27**, 28707–28721 (2019).

⁶⁵D. Ichikawa, W. Gao, N. H. Ngo, T. Ohara, M. Tanaka, S. Murakami, Y. Yamada, H. Yamane, Y. Nishida, M. Fujita, and T. Nagatsuma, “Terahertz on-chip communications with hybrid electronic-photonic interconnects,” *IEEE Trans. Terahertz Sci. Technol.* **15**, 751–762 (2025).

⁶⁶J. Webber, Y. Yamagami, G. Ducournau, P. Sriftgiser, K. Iyoda, M. Fujita, T. Nagatsuma, and R. Singh, “Terahertz band communications with topological valley photonic crystal waveguide,” *J. Lightwave Technol.* **39**, 7609–7620 (2021).

⁶⁷X. Ding, H. Yu, S. Sabbaghi, and Q. J. Gu, “A 1.6pJ/b 65Gb/s Si-dielectric-waveguide based multi-mode multi-drop sub-THz interconnect in 65nm CMOS,” in *2023 IEEE Custom Integrated Circuits Conference (CICC)* (2023) pp. 1–2.

⁶⁸M. Gupta, A. Kumar, P. Pitchappa, Y. J. Tan, P. Sriftgiser, G. Ducournau, and R. Singh, “150 Gbps THz Chipscale Topological Photonic Diplexer,” *Adv. Mater.* **36**, 2309497 (2024), <https://advanced.onlinelibrary.wiley.com/doi/10.1002/adma.202309497>.

Supplementary information

Terahertz Communications Using Effective-Medium-Slot Waveguides

Nguyen H. Ngo^{1,*}, Weijie Gao¹, Guillaume Ducournau², Hadjer Nihel Khelil², Rita Younes², Pascal Sriftgiser³, Hidemasa Yamane⁴, Yoshiharu Yamada⁴, Shuichi Murakami⁴, Withawat Withayachumnankul⁵, Masayuki Fujita¹

¹ Graduate School of Engineering Science, The University of Osaka, Toyonaka 560-8531, Japan

² CNRS, UMR 8520 – IEMN, Institut d’Electronique de Microélectronique et de Nanotechnologie, Université de Lille, Lille 59000, France

³ Laboratoire de Physique des Lasers, Atomes et Molécules, UMR CNRS 8523 PhLAM, Université de Lille, Lille 59000, France

⁴ Osaka Research Institute of Industrial Science and Technology, Osaka 594-1157, Japan

⁵ Terahertz Engineering Laboratory, Adelaide University, Adelaide SA 5005, Australia

* ngo.h-nghuyen.es@osaka-u.ac.jp

1. Alignment test

In conventional tapered spike designs, wave coupling occurs inside the core of the metallic hollow waveguide to the silicon taper, achieving high coupling efficiency. Maintaining precise alignment of tapered spikes is practically challenging, as deviations of only tens of micrometers can significantly degrade coupling efficiency. For example, [S1] reports simulated transmission coefficients ($|S_{21}|$) of 80–90%, whereas measured values after packaging drop to approximately 50%. Achieving perfect alignment typically requires meticulous manual adjustment under a microscope. In contrast, coupling to the proposed substrateless slot waveguide, which is completely outside the hollow core, results in partial energy leakage at the interface, slightly reducing transmittance. However, $|S_{21}|$ in this configuration is significantly less sensitive to misalignment than in the tapered-spike design. To elaborate the robustness of the substrateless slot waveguide for practical implementation, we compare the transmittance performance of the two structures through simulations.

Model explanation

Simulation models for the effective-medium (EM)-clad waveguide and the EM-slot waveguide are shown in Fig. S1(a,b). Misalignment offsets along the z -, x -, and y -axes are represented in the top, middle, and bottom rows, respectively. The TE mode (E_{11}^x) was excited at a WR-2.2 hollow waveguide port (559 $\mu\text{m} \times 279 \mu\text{m}$). The taper length of the EM waveguide was 25 mm, and the EM-slot waveguide dimensions are provided in Fig. 3 of the main text. For the z -axis (propagation direction), the distance between the hollow-waveguide interface and the tapered spike edge was set to 300 μm to avoid strong reflections caused by metal proximity to the cladding. For the EM-slot waveguide, the offset was set to 0 μm , ensuring direct contact between the hollow waveguide opening and the silicon slot coupler. Offsets along other axes were set to 0 μm , positioning the silicon waveguides at the hollow core center.

Simulation results

In the z -axis (top row, Fig. S1(c,d)), the optimal position for the slot coupler is located directly at the interface edge, eliminating the need for fine alignment. Meanwhile, the tapered-spike waveguide showed ripples in $|S_{21}|$ of approximately 1–2 dB, requiring

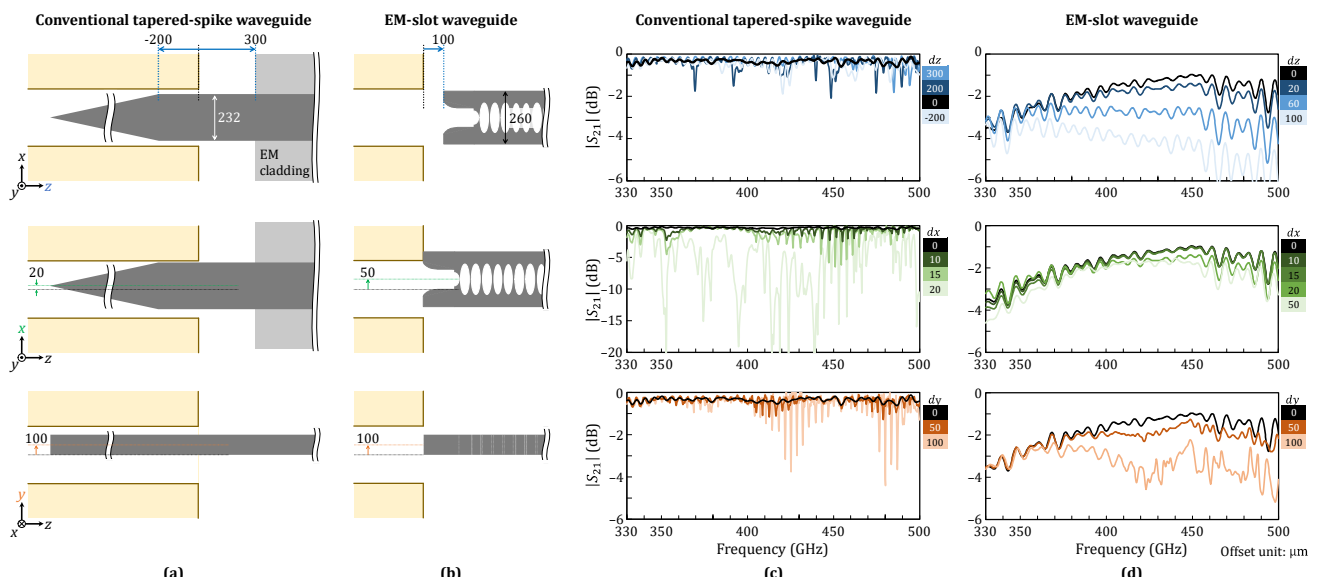


Fig. S1. Simulation models for misalignment offsets of (a) conventional tapered-spike waveguide and (b) effective-medium (EM)-slot waveguide. Simulated transmission coefficients of the corresponding misalignment along three axes for (c) conventional tapered-spike waveguide and (d) EM-slot waveguide. TE-mode (E_{11}^x) is excited at the hollow waveguide port. The misalignment in z -, x -, and y -axes are respectively presented in the top, middle, and bottom rows. The offset unit is in μm .

adjustment of positions for a flat response. Consequently, coupling efficiency of the tapered spike becomes challenging once the waveguide is fixed, such as after packaging or at frequencies approaching 1 THz [S1, S2].

Notably, the EM-slot waveguide exhibited negligible performance degradation for offsets up to 20 μm along the x -axis (middle row, Fig. S1(c,d)). Even if the offset extends to 50 μm , $|S_{21}|$ showed a slight degradation of less than 1-dB in the high-frequency range. In contrast, the tapered spike revealed significant transmittance reduction, with multiple ripples even at a 10- μm offset. At 20 μm , $|S_{21}|$ decreased dramatically less than -10 dB, likely due to strong field interference within the narrow gap between the metallic wall and silicon core.

For out-of-plane (y -axis) misalignment (bottom row, Fig. S1(c,d)), the tapered spike again demonstrated greater sensitivity compared to the EM-slot waveguide. When the offset was 100 μm , the ripples appeared in the conventional waveguide, decreasing the 3-dB bandwidth. In the EM-slot waveguide suffered approximately 2 dB in the high-frequency ranges because of the mode mismatch. Nevertheless, the 3-dB bandwidth was maintained the whole WR-2.2 band.

Practically, alignment tolerances of approximately ± 50 μm in both x - and y -directions are acceptable for the EM-slot waveguide, while the offset can be controlled under 20 μm using microscopes. Additionally, the EM-slot does not require the z -axis adjustment. Overall, the EM-slot waveguide exhibits superior robustness to misalignment, making it a promising candidate for integration with hollow-waveguide interface and scalable packaging.

2. The utilization of the THz substrateless slot waveguide for interconnects

The substrateless slot waveguide with taper-free couplers enables robust coupling to hollow-waveguide-based devices without a fragile tapered spike, reducing the fine micro-machining required for conventional silicon waveguides. However, since the effective-medium channel consists of elliptical air holes, it is difficult to implement bending or furcating structures [S3-S5]. To address this limitation, simplifying the air holes by gradually transforming the hole size to a homogenous silicon channel can retain the slot interface while the channel can be flexibly designed with various shapes. Figure S2(a) illustrates the EM-slot waveguide with progressively reduced air-hole sizes, decreasing from 100% to 10% in steps of 10%. The coupling efficiency of this modified structure reaches approximately 90%, comparable to that of the original EM-slot waveguide as evidenced with an average difference of only 0.17 dB. The wavy coupling efficiency is likely due to the limited discrete changes of the effective refractive index (n_{eff}) along the modification region. This can be solved by optimizing the sizes or increasing the number of reduced-size air holes, obtaining smoother change of n_{eff} .

Consequently, the modified EM-slot waveguide can be potentially applied as a silicon platform with various functions, such as waveguides, multiplexers, and rotators. With the simple integration with THz active devices, the waveguide can be used for hybrid (electrical-THz-optical)-interconnection devices, such as an RTD module or a packaged UTC-PD [S1, S6], as conceptually visualized by Fig. 1 of the main text.

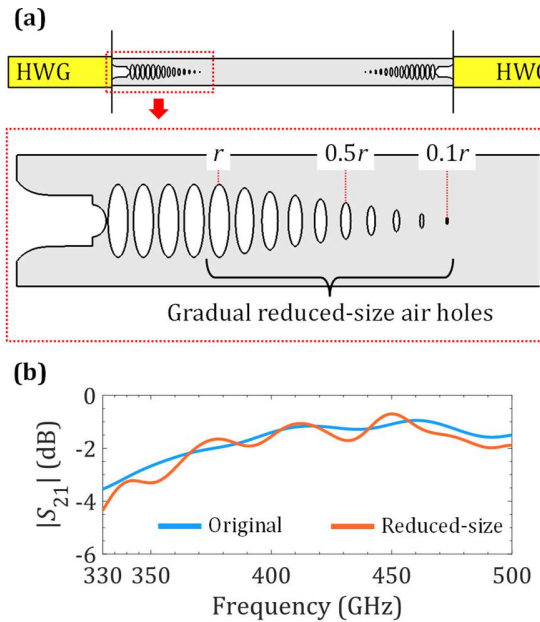


Fig. S2. Substrateless slot waveguide transition. (a) EM-slot channel with gradual reduced-size air holes. The radius of each ellipse shrinks by 10% of the original ellipse's radius, from 100% to 10%. (b) Coupling efficiencies of the original EM-slot waveguide (blue) and the gradual reduced-size air-hole waveguide (orange).

References

- [S1] N.H. Ngo, Y. Inose, Y. Kawamoto, Y. Nishida, M. Fujita, and T. Nagatsuma, "WR-2.2-band (330-500 GHz) packaged resonant tunneling diode receiver module for terahertz communications," in *2023 Asia-Pacific Microwave Conference (APMC)*, (2023), pp. 399–401.
- [S2] R. Koala, R. Maru, K. Iyoda, L. Yi, M. Fujita, and T. Nagatsuma, "Ultra-low-loss and broadband all-silicon dielectric waveguides for WR-1 band (0.75–1.1 THz) modules," *Photonics* **9**(8), 515 (2022).
- [S3] R.A.S.D. Koala, M. Fujita, and T. Nagatsuma, "Nanophotonics-inspired all-silicon waveguide platforms for terahertz integrated systems," *Nanophotonics* **11**(9), 1741–1759 (2022).
- [S4] Z. Tan, Q.-Y. Zhang, Y.-L. Lei, Y. Zhao, and J.-Q. Ding, "Terahertz waveguide multiplexers: A review," *Microwave and Optical Technology Letters* **65**(7), 1925–1935 (2023).
- [S5] D. Headland, M. Fujita, G. Carpintero, T. Nagatsuma, and W. Withayachumnankul, "Terahertz integration platforms using substrateless all-silicon microstructures," *APL Photonics* **8**(9), 91101 (2023).
- [S6] T. Ohara, T. Ishibashi, Y. Kawamoto, M. Tojo, K. Maekawa, and T. Nagatsuma, "2-mW-output power uni-traveling-carrier photodiodes in 300-GHz-Band," in *2023 Asia-Pacific Microwave Conference (APMC)*, (2023), pp. 676–678.